

Enhancing Photon Identification with Neural Network Methods

Yuval Frid and Liron Barak

Tel Aviv University, Tel Aviv-Yafo, Israel

Abstract

We investigate photon–pion discrimination in regimes where electromagnetic showers overlap at the scale of calorimeter granularity. Using full detector simulations with fine-grained calorimeter segmentation of approximately 0.025×0.025 in (η, ϕ) , we benchmark three approaches: boosted decision trees (BDTs) on shower-shape variables, dense neural networks (DNNs) on the same features, and a ResNet-based convolutional neural network operating directly on calorimeter cell energies. The ResNet significantly outperformed both baseline methods, achieving further gains when augmented with soft scoring and an auxiliary ΔR regression head. Our results demonstrate that residual convolutional architectures, combined with physics-informed loss functions, can substantially improve photon identification in high-luminosity collider environments in which overlapping electromagnetic showers challenge traditional methods.

1 Introduction

The Large Hadron Collider (LHC) has enabled precision measurements of Standard Model processes and opened new frontiers in the search for physics beyond the Standard Model. Central to many of these studies is the accurate identification of photons, which provide relatively clean experimental signatures in the high-multiplicity environment of hadron collisions. The clean signature of photons in hadron colliders has made them a powerful probe for precision measurements and searches for new physics [1, 2]. Therefore, accurate reconstruction and identification of photons is a crucial task in high-energy physics experiments [3]. Photon candidates are identified and reconstructed using calorimeter and tracker information. Due to the nature of photon interactions in the calorimeter – namely, pair production and bremsstrahlung – a photon entering the detector produces a cascade of secondary particles, forming an electromagnetic (EM) shower [4].

Traditionally, EM showers are characterized using a set of carefully engineered observables known as *shower-shape variables* [5]. Selection cuts or multivariate classifiers trained on these variables are employed to distinguish *prompt photons*, produced directly in the hard scattering process, from *non-prompt photons* originating from hadronic decays or fragmentation. In both the ATLAS and CMS experiments, boosted decision trees (BDTs) based on these shower-shape variables constitute the standard photon-identification algorithm [3, 5, 6]. These approaches

have demonstrated excellent performance across most kinematic regimes, but their discriminating power degrades in challenging conditions such as high pile-up (multiple overlapping proton–proton collisions in the same bunch crossing) or when EM showers become spatially overlapping at fine calorimeter granularity. In recent years, machine learning techniques have increasingly been explored for photon and electron identification, aiming to surpass the limitations of handcrafted shower-shape variables. Early studies by the ATLAS and CMS collaborations demonstrated that deep neural networks trained on calorimeter observables can improve discrimination power compared to traditional BDT-based approaches [7, 8]. Further work has extended these ideas to more expressive architectures such as convolutional neural networks (CNNs) operating directly on calorimeter cell images [9, 10], or hybrid models combining high-level variables with low-level features [11, 12]. Collectively, these studies highlight the growing potential of deep learning in EM shower classification tasks. However, despite these advances, a persistent challenge in photon identification remains: the discrimination of neutral pion (π^0) decays that mimic single-photon signatures.

A notable difficulty arises from the presence of π^0 mesons, which decay to two photons in over 98% of cases [13]. For a π^0 mass of ~ 135 MeV and photon energies in the GeV range, the opening angle θ between the two decay photons is typically very small [3, 13]. This understanding follows from the invariant mass relation for massless photons:

$$M_{\pi^0}^2 = 2E_{\gamma_1}E_{\gamma_2}(1 - \cos\theta), \quad (1)$$

which shows that higher-energy photons correspond to smaller opening angles. As a result, the two decay photons can be highly collimated, sometimes depositing their energy in overlapping regions of the calorimeter, making them difficult to distinguish from single photons (see Fig. 1) [3].

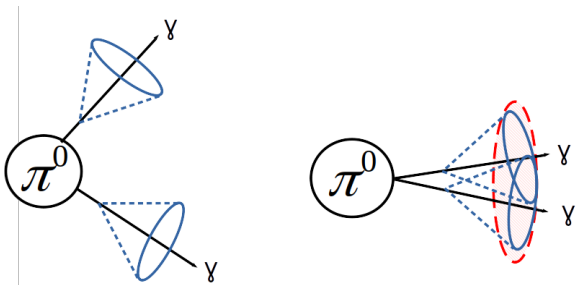


Figure 1: Illustration of π^0 decay to two photons for well-separated and highly collimated cases.

In this work, we investigate the use of deep neural networks for photon identification in a challenging kinematic regime where standard techniques exhibit reduced performance: photon energies between 10 and 100 GeV, where collimated π^0 decays are most problematic. Simulated samples are generated with the COCOA-HEP library [14], which couples PYTHIA8 [15] event generation with full detector simulation in Geant4 [16]. The calorimeter was configured with three layers in both the electromagnetic and hadronic sections. The EM1 and EM2 layers have

nearly symmetric granularity of approximately 0.025×0.025 in (η, ϕ) , with exact segmentation shown in Table 1. This near-uniform segmentation provides a suitable two-dimensional shower representation for convolutional neural network studies.

We benchmark three complementary approaches: (i) the standard shower-shape variables with a BDT baseline [3], (ii) a dense neural network trained on the same high-level inputs, and (iii) a ResNet-based convolutional network trained directly on calorimeter images. Additionally, we explore the impact of separating background events according to their diphoton separation ΔR , investigating whether dedicated training for events with $\Delta R < 0.025$ yields further performance gains. While earlier studies have primarily addressed photon–electron or photon–jet separation using deep learning, the present work focuses specifically on the challenging case of $\pi^0 \rightarrow \gamma\gamma$ overlaps at high calorimeter granularity. In addition, we introduce two physics-informed strategies – soft scoring and an auxiliary ΔR regression head—that guide the network toward spatially discriminative features beyond those employed in previous approaches.

2 Monte Carlo Sample Generation

For this study, a calorimeter simulation with high transverse and longitudinal granularity was utilized to perform photon identification (PID) using a CNN on detailed shower-shape information. While fast-simulation frameworks such as DELPHES [17] can be configured to achieve a transverse segmentation comparable to the one used here (down to $\eta \times \phi$ cells of 0.025×0.025 or finer), they are inherently limited to a single EM and a single hadronic calorimeter layer [18, 19]. These layers are modeled as 2D energy maps derived from parameterized detector resolutions, lacking a realistic longitudinal shower development. As a result, multi-layer correlations, depth-dependent energy patterns, and realistic shower-shapes cannot be reproduced. Such information is essential for CNN-based PID, making DELPHES inadequate for the purposes of this study.

Instead, we utilized the COCOA-HEP detector simulation [14], which provides full 3D calorimeter modeling with multiple configurable layers, per-cell energy deposits, and realistic shower evolution. The collision and detector parameters were chosen to be broadly consistent with ATLAS in terms of magnetic field, radiation length, and $\sqrt{s} = 14$ TeV, corresponding to the design energy of the High-Luminosity LHC phase in which future photon identification studies will operate. The calorimeter was configured with three layers in both the EM and hadronic sections, each with uniform $\eta \times \phi$ segmentation as shown in Table 1.

2.1 Signal Samples

Signal events were generated from five prompt-photon production processes: $qg \rightarrow q\gamma$, $qq \rightarrow g\gamma$, $qq \rightarrow \gamma\gamma$, $gg \rightarrow g\gamma$, and $gg \rightarrow \gamma\gamma$ [15]. A minimum hard-scatter transverse momentum (pTHatMin) of 10 GeV was applied, and only photons with $10 < p_T < 100$ GeV were retained. The energy range between 10 and 100 GeV was selected as this is the most challenging regime for photon identification. Above 100 GeV, identification efficiency saturates at a high

COCOA Calorimeter Layer	$\eta \times \phi$ granularity
EM1	0.025×0.0245
EM2	0.025×0.0245
EM3	0.050×0.0491
HAD1	0.100×0.0982
HAD2	0.100×0.0982
HAD3	0.200×0.1965

Table 1: Cell granularity in the calorimeter layers in $\eta \times \phi$. The ϕ segmentation reflects equal angular divisions of 2π , resulting in values slightly different from the nominal η spacing.

plateau[3]; while below 10 GeV, EM showers are often too small and poorly contained to be reliably separated from hadronic backgrounds, making photon identification practically impossible under realistic detector conditions [3, 5]. From the full generated dataset, 1.1 million events were selected to produce a flat p_T spectrum, avoiding the over-representation of low- p_T photons inherent in the original steeply falling distribution. The dataset was then split into 70% for training and validation, and 30% for testing.

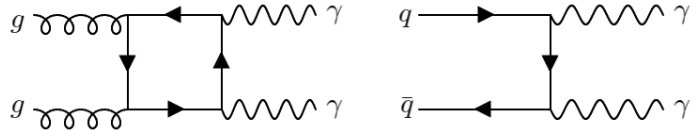


Figure 2: The two main channels for direct diphoton production at the LHC.

2.2 Background Samples

Background events were generated from all QCD processes, requiring at least one π^0 in the final state with $10 < p_T < 100$ GeV, decaying into two photons [15, 13]. distribution of ΔR between the two photons is shown in figure 4, with two thirds of the diphoton pairs having $\Delta R < 0.025$, lower than the detector's resolution. Unlike the signal, no p_T reweighting was performed on the background, preserving the true steeply falling QCD spectrum in which low- p_T events dominate.

A minimum hard-scatter transverse momentum (pTHatMin) of 10 GeV was applied [15]. Unlike the signal, no p_T reweighting was performed on the background. This decision preserves the true steeply falling QCD p_T spectrum, which is essential because the background classifier must be trained to reject events across the realistic, dominant low- p_T phase space observed in experimental data.

In total, 4.2 million background events were produced, with 900k used for training and validation, while 3.3 million were reserved for testing. A large test set is essential because, after applying the selection criteria for both signal and background, π^0 decays occur roughly 1,000 times more frequently than prompt-photon processes. As a result, performance is evaluated in the $\sim 0.1\%$ fake-rate regime, corresponding with a realistic scenario where the signal-to-background ratio approaches unity after selection.

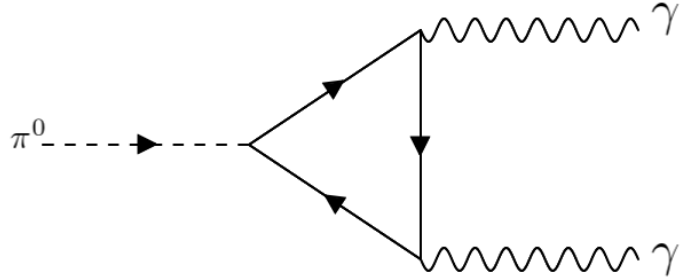


Figure 3: π^0 decay into two photons.

The number of events used at each stage is summarized in Table 2.

Sample Type	Training	Validation	Test
Signal	682,470	113,670	341,370
Background	700,000	200,000	3,300,000

Table 2: Event counts for each dataset split.

3 Methods

3.1 Shower-Shape and BDT Baseline

Algorithms currently used for object classification in collider experiments are often referred to as Cut-Based algorithms. For each object, a set of shower-shape variables is calculated, and a multi-dimensional cut is optimized to select signal objects at a given fake-positive rate. In practice, modern implementations frequently use a Boosted Decision Tree (BDT) trained on the same variables instead of a literal cut-flow. In this work, we implement the BDT as baseline, using `XGBoost` [20]. The 20 shower-shape variables used in this work are based on those employed in ATLAS photon identification analyses [5] and are listed in Table 3.

Variable Name	Description
R_{had}	Ratio of E_T in hadronic layers over E_T in EM layers
I_{so}	Ratio of $12 \times 12 E_T$ sum over $20 \times 20 E_T$ sum
F_{EMX}	Ratio of E_T sum in EM_X over sum in all layers
R_η	Ratio of $3 \times 7 E_T$ sum over $7 \times 7 E_T$ sum
R_ϕ	Ratio of $3 \times 3 E_T$ sum over $3 \times 7 E_T$ sum
$W_{\eta 2}$	Second moment of η in 3×5 cells: $\sqrt{(\sum E_i \eta_i^2)/(\sum E_i) - ((\sum E_i \eta_i)/(\sum E_i))^2}$
E_{ratio}	Ratio between difference of two maximum cells over their sum
E_{dR}	ΔR distance between two maximum cells

Table 3: Shower-shape variables for Cut-Based and BDT algorithms. All $A \times B$ rectangles are in $\eta \times \phi$ space. A single 1×1 cell corresponds to 0.025×0.0245 in (η, ϕ) .

The first two variables are per sample, while the last six are per EM layer, resulting in 20 variables in total.

3.2 Dense Neural Network Baseline

To provide a direct comparison with the BDT, we also implement a Dense Neural Network (DNN) trained on the same twenty shower-shape variables. This baseline, implemented in PyTorch [21], is designed to have a comparable number of trainable parameters to the BDT, ensuring that differences in performance are due to model architecture rather than capacity. The DNN consists of several fully connected layers with ReLU activations and dropout for regularization, as shown in 9.

3.3 CNN/ResNet Calorimeter-Based Model

Our primary approach uses calorimeter cell information directly, without engineered features. Due to the different granularities of the EM and Had calorimeters (Table 1), they are treated as two separate input branches:

- **EM branch:** Three layers, with the last one upsampled so that the coarsest layer matches the resolution of the others. An ROI of 0.3×0.295 in (η, ϕ) was selected, resulting in a $3 \times 12 \times 12$ tensor.
- **Had branch:** Similarly upsampled, producing a $3 \times 3 \times 3$ tensor.

Each branch is processed through a sequence of residual convolutional blocks (*ResNet blocks*), allowing the network to learn deep spatial features without vanishing gradients. The outputs of the EM and Had branches are flattened, concatenated, and passed through fully connected layers for classification, as shown in 10. This two-prong ResNet-based architecture, implemented in PyTorch [21] and using residual blocks [22], is designed to exploit spatial correlations in the calorimeter data, which are inaccessible to cut-based or shower-shape approaches.

3.4 Additional Training Strategies

Beyond the baseline ResNet architecture, we explored two complementary strategies aimed at improving performance in challenging background regimes.

Soft scoring scheme Background events with photon pairs at very small angular separation ($\Delta R < 0.025$) are particularly difficult to reject due to their high similarity to true photon showers. To encourage the network to better separate these cases, we implemented a *soft scoring* scheme (also known as label smoothing) [23, 24] in which such background events are assigned continuous target labels between 0 and 1 rather than a hard zero, as shown in 4. This smooth target transition reduces the loss penalty for near-misses and allows the model to focus its capacity on improving discrimination where it is most needed. Following multiple tests, the Fermi-Dirac (FD) function in the range [0,0.4] achieved the best results.

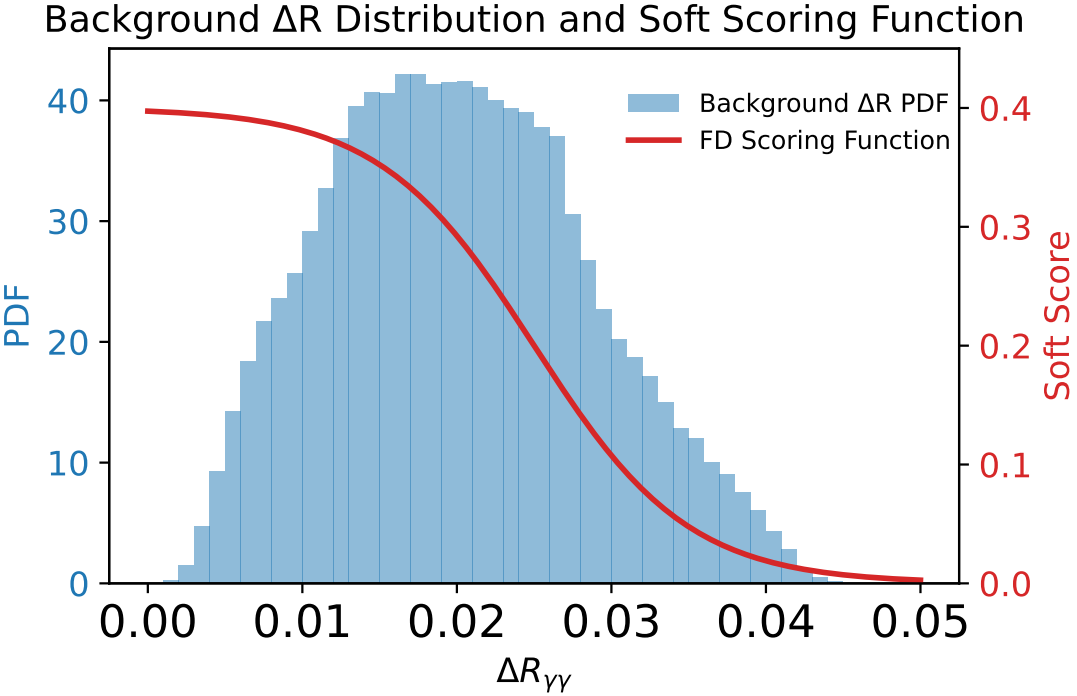


Figure 4: Distribution of ΔR between photon pairs from π^0 decay (blue histogram, left axis) and the corresponding soft-scoring target function (red curve, right axis). Background events were assigned continuous labels between 0 and 0.4 using a Fermi-Dirac-inspired function, reducing the penalty for near-threshold cases while maintaining hard labels for well-separated pairs.

Auxiliary ΔR head We further added an auxiliary output branch that predicts the ΔR of background photon pairs [25], as shown in 11. This branch shares the same convolutional backbone as the main classifier but has its own regression head, contributing an auxiliary loss term during training. The predicted ΔR does not contribute to the final classification score, as it is highly correlated with the output score. Rather, it serves as an additional supervision signal to guide the feature extractor towards representations sensitive to small-scale spatial differences. This multi-task setup proved effective in regularizing the network and improving robustness, especially for closely spaced photon pairs.

4 Results

This section presents the performance of the algorithms introduced in Section 3. We first compare the baseline approaches — shower-shape-based BDT, a DNN with the same inputs, and a calorimeter-based ResNet — to quantify the gain from using full calorimeter information. We then evaluate refinements to the ResNet, including the soft-scoring approach and the auxiliary ΔR head. Finally, performance is shown separately for two background topologies, defined by $\Delta R < 0.025$ and $\Delta R \geq 0.025$ between the two photons from π^0 decay.

4.1 Baseline performance: BDT, DNN, and ResNet

Figure 5 shows the ROC curves for the three baseline models, focusing on the background efficiency range $10^{-4} \leq \epsilon_{\text{bkg}} \leq 10^{-2}$. This range corresponds to the high-purity regime relevant for photon identification at the LHC. The ResNet significantly outperforms both the BDT and the DNN across the entire range, achieving higher signal efficiency at fixed background efficiency.

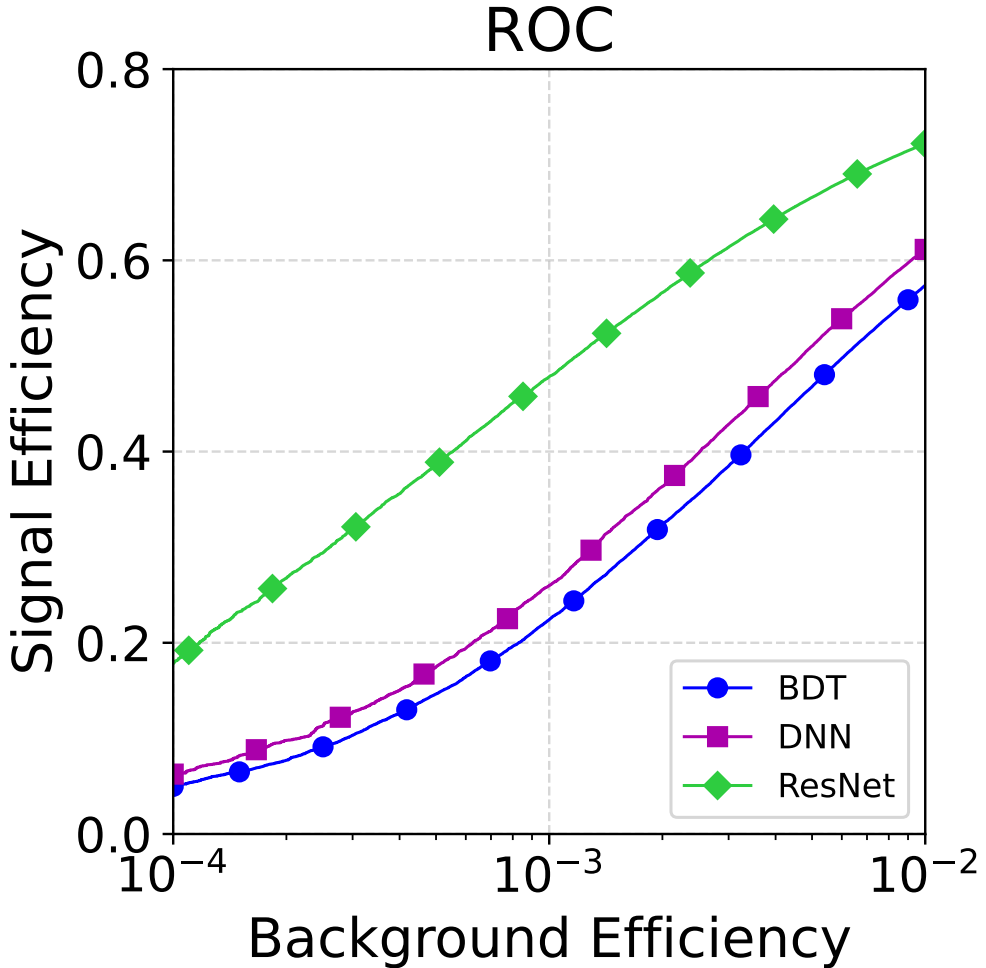


Figure 5: ROC curves for BDT, DNN, and ResNet, shown in the high-purity regime ($10^{-4} \leq \epsilon_{\text{bkg}} \leq 10^{-2}$). The ResNet (top curve) demonstrates superior performance than BDT and DNN, achieving higher signal efficiency at any given background efficiency, with the performance gap widening at lower background efficiencies (higher purity).

The turn-on curves in Figure 6 illustrate signal efficiency as a function of true p_T for fixed background rejection rates (1%, 0.1%, and 0.01%). The ResNet maintains a steeper turn-on and higher plateau efficiency than either the BDT or DNN, particularly at low p_T , where shower-shape variables alone are less discriminating.

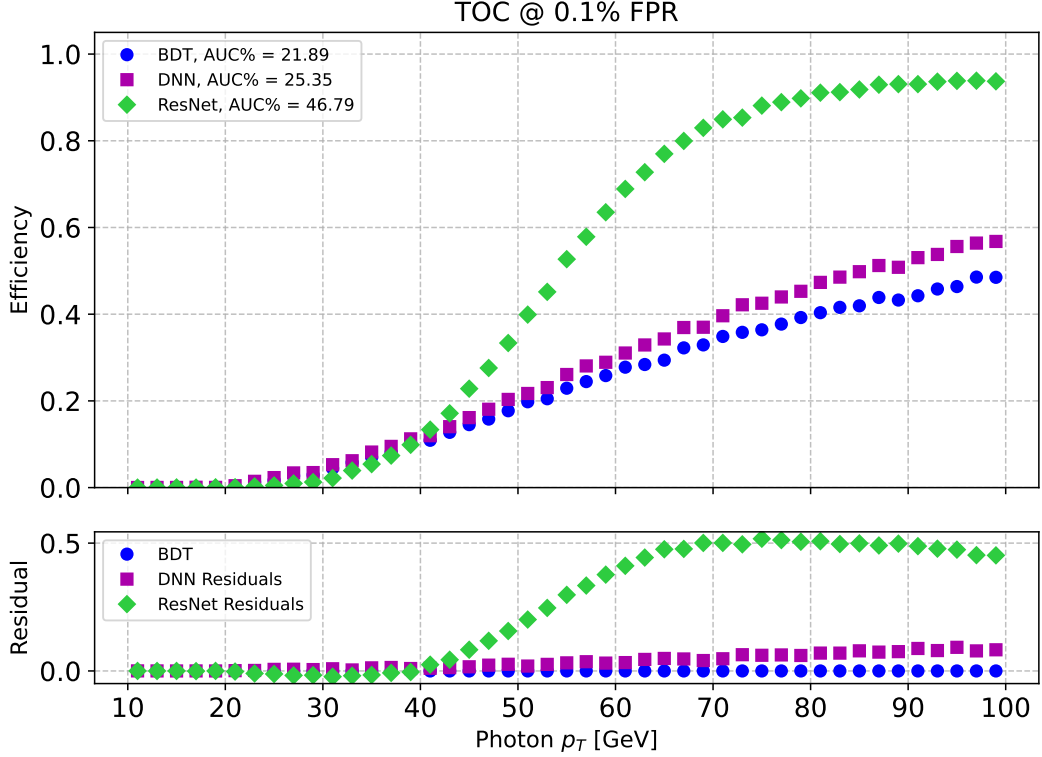


Figure 6: Turn-on curves for BDT, DNN, and ResNet, showing signal efficiency vs. true p_T at 0.1% false positive. The ResNet achieves a steeper turn-on and higher plateau efficiency than either of the other options, particularly at low p_T , indicating more robust identification across the kinematic range.

4.2 ResNet refinements: Soft scoring and ΔR auxiliary head

Next, we compare the baseline ResNet with two refinements:

1. **Soft scoring:** the network is trained with a softened target for events in the hard-background region, improving separation power without explicitly using ΔR as an input.
2. **ΔR auxiliary head:** an additional regression head predicts ΔR and contributes to the loss function, providing a physics-informed inductive bias.

Figure 7 shows that both refinements lead to measurable gains in the high-purity regime. The improvement is most pronounced for the hard-background subset, as quantified in Section 3.4.

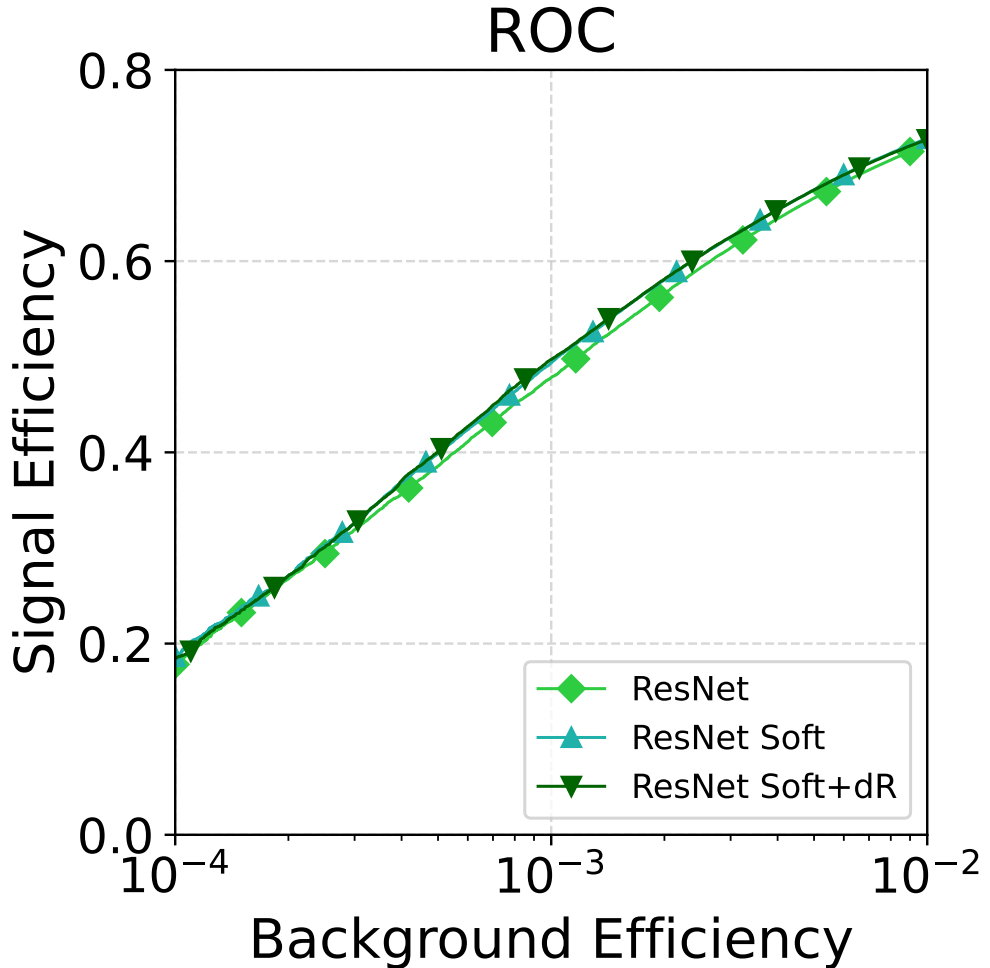


Figure 7: ROC curves for baseline ResNet, soft scoring ResNet and ResNet with auxiliary ΔR head shown in the high-purity regime ($10^{-4} \leq \epsilon_{\text{bkg}} \leq 10^{-2}$). While all models converge at the highest purity ($\epsilon_{\text{bkg}} \approx 10^{-4}$), the refined models show consistent improvements in the 10^{-3} background efficiency regime, demonstrating enhanced discrimination for challenging background events

Figure 8 shows the corresponding turn-on curves. The soft-scoring approach shifts the turn-on to lower p_T , while the auxiliary head further improves efficiency in the low- p_T region.

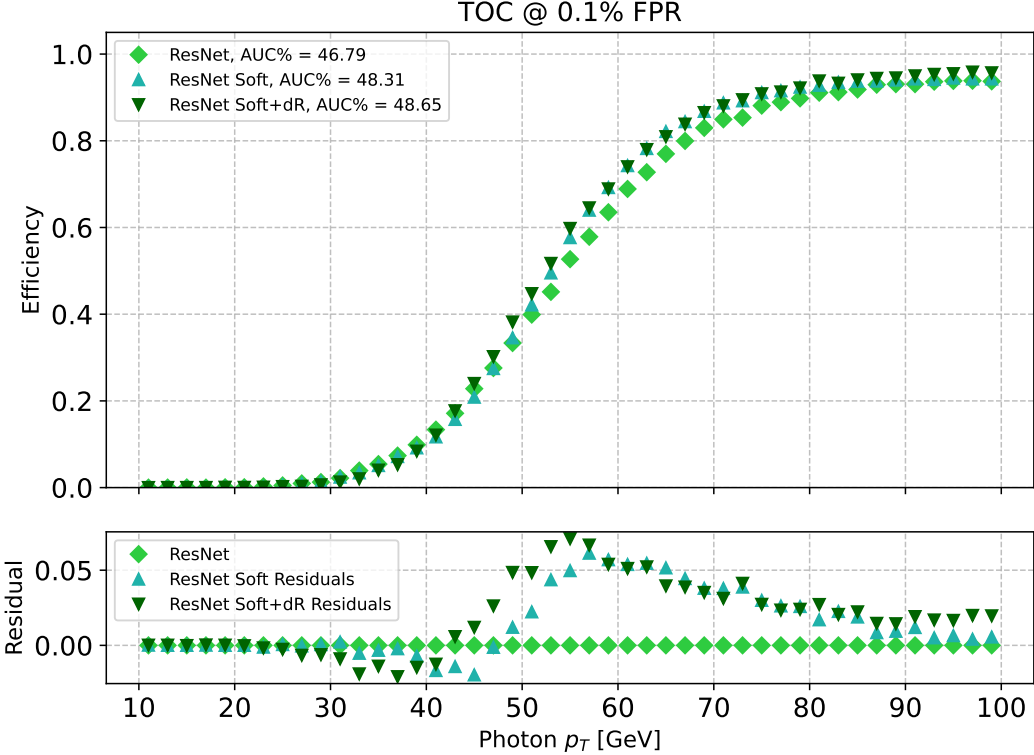


Figure 8: Turn-on curves for the ResNet and its refinements. The soft-scoring strategy shifts the turn-on to lower p_T , while the auxiliary ΔR head further enhances the low p_T efficiency, demonstrating that both techniques help the model better identify signal photons in the most challenging kinematic region.

Turn-on curves, displayed in the lower inset panel, show the signal efficiency vs. true p_T at 0.1% false positive rate for the three DualResNet training strategies. The soft scoring approach (ResNet Soft) achieves a significant increase in overall performance (AUC from 46.79% to 48.31%) with similar high-end saturation. Furthermore, adding the ΔR Auxiliary Head (ResNet Soft+ ΔR) provides another slight improvement (AUC = 48.65%), maintaining the robust, high-plateau efficiency.

5 Conclusions

In this study, we generated and simulated photon and pion samples using the COCOA-HEP tool, a state-of-the-art detector simulation framework. We emulated the current baseline method for photon identification, a BDT classifier based on shower-shape variables, and introduced DNN and ResNet architectures as the natural next step toward improved performance.

Our results demonstrate that the ResNet significantly outperforms both the BDT and DNN across key metrics, particularly in the very low false-positive rate regime relevant for high-purity photon identification. Furthermore, we showed that fine-tuning with soft scoring and incorporating angular separation information leads to additional gains, enabling the model to better discriminate the most challenging background cases without sacrificing signal efficiency.

These findings highlight the potential of modern deep learning architectures, combined with physics-informed loss functions, to improve photon identification in collider experiments. Future work could extend these methods to full detector simulations and explore applications for real experimental data.

In contrast to previous deep-learning-based photon identification studies, which largely emphasized global shower properties or jet discrimination, our approach explicitly targets the sub-structure of overlapping electromagnetic showers in a symmetric calorimeter geometry. This method provides a clean, controlled benchmark for future photon identification developments at the High-Luminosity LHC and beyond.

6 Acknowledgements

The work of Y.F and L.B is supported by an ERC STG grant ('BoostDiscovery', grant No.945878). We thank Dr. Rachel Jordan Hyneman and Dr. Luis Pascual Dominguez for their constructive feedback.

Appendix

A Model Architectures

This appendix provides detailed architectural diagrams for the neural network models described in Section 3.

A.1 Dense Neural Network

Figure 9 shows the fully connected DNN architecture used as a baseline comparison to the BDT. The network consists of four fully connected layers with batch normalization, ReLU activations, and dropout regularization.

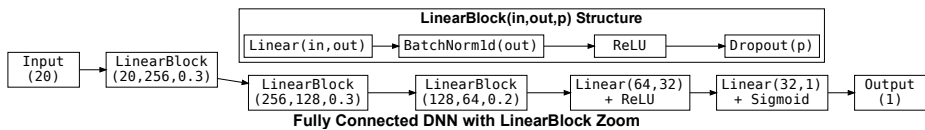


Figure 9: Dense neural network architecture with LinearBlock components. Each LinearBlock consists of a linear layer, batch normalization, ReLU activation, and dropout with probability p .

A.2 ResNet Calorimeter Model

Figure 10 illustrates the dual-branch ResNet architecture that processes electromagnetic (EM) and hadronic (HAD) calorimeter inputs separately before fusion.

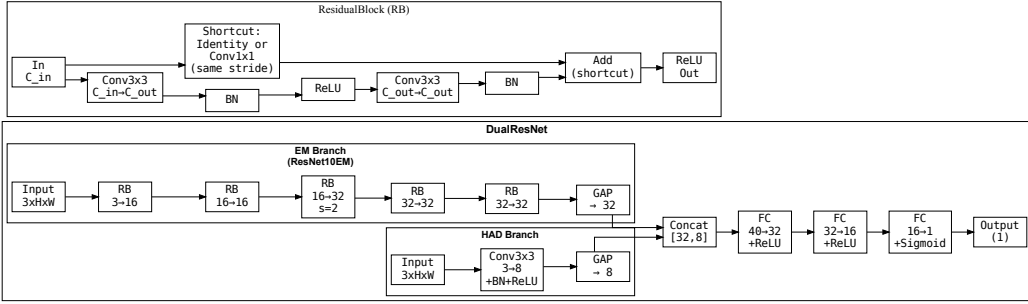


Figure 10: DualResNet architecture with separate processing branches for EM and HAD calorimeter layers. Each branch uses residual blocks (RB) with skip connections. GAP = Global Average Pooling; BN = Batch Normalization.

A.3 ResNet with Auxiliary Head

Figure 11 shows the multi-task extension with an auxiliary ΔR regression head that shares the convolutional backbone.

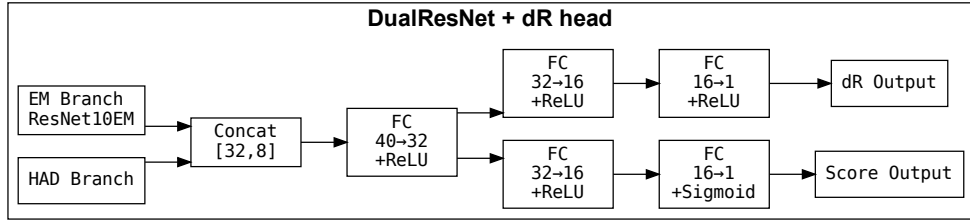


Figure 11: DualResNet with auxiliary ΔR prediction head. The regression output provides additional supervision during training but is not used for final classification.

References

- [1] ATLAS Collaboration, “Observation of a new particle in the search for the Standard Model Higgs boson with the ATLAS detector at the LHC,” *Phys. Lett. B*, vol. 716, pp. 1–29, 2012.
- [2] CMS Collaboration, “Observation of a new boson at a mass of 125 GeV with the CMS experiment at the LHC,” *Phys. Lett. B*, vol. 716, pp. 30–61, 2012.
- [3] ATLAS Collaboration, “Electron and photon performance measurements with the ATLAS detector using the 2015–2017 LHC proton–proton collision data,” *JINST*, vol. 14, no. 12, p. P12006, 2019.
- [4] W. R. Leo, *Techniques for Nuclear and Particle Physics Experiments: A How-to Approach*. Springer, 1994.
- [5] ATLAS Collaboration, “Measurement of the photon identification efficiencies with the ATLAS detector using LHC Run 2 data collected in 2015 and 2016,” *Eur. Phys. J. C*, vol. 79, no. 3, p. 205, 2019.
- [6] C. Collaboration, “Electron and photon reconstruction and identification with the cms experiment at the cern lhc,” 2020.
- [7] “Photon identification with convolutional neural networks in atlas,” Tech. Rep. ATL-PHYS-PUB-2019-028, ATLAS Collaboration, 2019.
- [8] “Performance of a deep neural network for photon identification,” Tech. Rep. CMS-DP-2019-007, CMS Collaboration, 2019.
- [9] L. de Oliveira, M. Paganini, and B. Nachman, “Learning particle physics by example: Electron vs. photon showers,” *JHEP*, vol. 07, p. 069, 2016.
- [10] B. Accettura *et al.*, “Shower identification in high-granularity calorimeters using deep learning,” *Eur. Phys. J. C*, vol. 83, p. 261, 2023.
- [11] J. Duarte *et al.*, “Fast inference of deep neural networks in fpgas for particle physics,” *JINST*, vol. 13, p. P07027, 2018.
- [12] P. Komiske, E. Metodiev, and J. Thaler, “Energy flow networks: Deep sets for particle jets,” *JHEP*, vol. 01, p. 121, 2019.
- [13] Particle Data Group, “Review of Particle Physics,” *Prog. Theor. Exp. Phys.*, vol. 2024, no. 8, p. 083C01, 2024.
- [14] F. A. D. Bello, A. Charkin-Gorbulin, K. Cranmer, E. Dreyer, S. Ganguly, E. Gross, L. Heinrich, L. Santi, M. Kado, N. Kakati, P. Rieck, and M. Tusoni, “Configurable calorimeter simulation for ai applications (cocoa),” 2023.

- [15] T. Sjostrand, S. Ask, J. R. Christiansen, R. Corke, N. Desai, P. Ilten, S. Mrenna, S. Prestel, C. O. Rasmussen, and P. Z. Skands, “An Introduction to PYTHIA 8.2,” *Comput. Phys. Commun.*, vol. 191, pp. 159–177, 2015.
- [16] S. Agostinelli *et al.*, “GEANT4: A Simulation toolkit,” *Nucl. Instrum. Meth. A*, vol. 506, pp. 250–303, 2003.
- [17] J. de Favereau *et al.*, “DELPHES 3, A modular framework for fast simulation of a generic collider experiment,” *JHEP*, vol. 02, p. 057, 2014.
- [18] ATLAS Collaboration, “Fast calorimeter simulation in ATLAS.” ATL-PHYS-PUB-2017-015, CERN, 2017. Accessed: 2025-10-10.
- [19] CMS Collaboration, “The CMS fast simulation of the detector,” *J. Phys. Conf. Ser.*, vol. 898, p. 022033, 2017.
- [20] T. Chen and C. Guestrin, “Xgboost: A scalable tree boosting system,” in *Proceedings of the 22nd ACM SIGKDD International Conference on Knowledge Discovery and Data Mining*, pp. 785–794, 2016.
- [21] A. Paszke, S. Gross, F. Massa, A. Lerer, J. Bradbury, G. Chanan, T. Killeen, Z. Lin, N. Gimelshein, L. Antiga, A. Desmaison, A. Kopf, E. Yang, Z. DeVito, M. Raison, A. Tejani, S. Chilamkurthy, B. Steiner, L. Fang, J. Bai, and S. Chintala, “Pytorch: An imperative style, high-performance deep learning library,” 2019.
- [22] K. He, X. Zhang, S. Ren, and J. Sun, “Deep residual learning for image recognition,” in *Proceedings of the IEEE Conference on Computer Vision and Pattern Recognition (CVPR)*, pp. 770–778, 2016.
- [23] C. Szegedy, V. Vanhoucke, S. Ioffe, J. Shlens, and Z. Wojna, “Rethinking the inception architecture for computer vision,” in *Proceedings of the IEEE Conference on Computer Vision and Pattern Recognition (CVPR)*, pp. 2818–2826, 2016.
- [24] R. Müller, S. Kornblith, and G. Hinton, “When does label smoothing help?,” 2020.
- [25] R. Caruana, “Multitask learning,” *Machine Learning*, vol. 28, pp. 41–75, 1997.